Commun. Comput. Phys.
doi: 10.4208/cicp.200114.090316a

Vol. **20**, No. 3, pp. 811-834
September 2016

A Contact Line Dynamic Model for a Conducting Water Drop on an Electrowetting Device

Dongdong He[1] and Huaxiong Huang[2,3,*]

[1] *School of Aerospace Engineering and Applied Mechanics, Tongji University, Shanghai, 200092, China.*
[2] *Department of Mathematics and Statistics, York University, Toronto, Ontario, M3J 1P3, Canada.*
[3] *Fields Institute, Toronto, Ontario, M5T 3J1, Canada.*

Communicated by Ming-Chih Lai

Received 20 January 2014; Accepted (in revised version) 9 March 2016

Abstract. The static shape of drop under electrowetting actuation is well studied and recent electrowetting theory and experiments confirm that the local contact angle (microscopic angle) is unaffected while the apparent contact angle (macroscopic angle) is characterized by the Lippmann-Young equation. On the other hand, the evolution of the drop motion under electrowetting actuation has received less attention. In this paper, we investigate the motion of a conducting water drop on an electrowetting device (EWD) using the level set method. We derive a contact line two-phase flow model under electrowetting actuation using energy dissipation by generalizing an existing contact line model without the electric field. Our model is consistent with the static electrowetting theory as the dynamic contact angle satisfies the static Young's equation under equilibrium conditions. Our steady state results show that the apparent contact angle predicted by our model satisfies the Lippmann-Young's relation. Our numerical results based on the drop maximum deformation agree with experimental observations and static electrowetting theory. Finally, we show that for drop motion our results are not as good due to the difficulty of computing singular electric field accurately. Nonetheless, they provide useful insights and a meaningful first step towards the understanding of the drop dynamics under electrowetting actuation.

AMS subject classifications: 76T99, 76W05, 65M06

Key words: Moving contact line, contact angle, level set method, electrowetting, slip conditions.

1 Introduction

Electrowetting devices (EWD) are gaining popularity in digital microfluidics as they can be used to create, transport, break up and merge drops [1–3] and transport heat [4].

*Corresponding author. *Email addresses:* dongdonghe@tongji.edu.cn (D. He), hhuang@yorku.ca (H. Huang)

 ©2016 Global-Science Press

https://doi.org/10.4208/cicp.200114.090316a Published online by Cambridge University Press

Electrowetting as a popular technique to manipulate droplets is introduced about two decades ago. Studies have been carried out to understand the steady-state droplet shape response to an external electric field. On the other hand, many microfluidic applications will benefit from a better understanding the dynamics of droplets under electrowetting actuation [5,6].

Contact line dynamics without electric field have been extensively studied both experimentally and theoretically, cf. [7] and references therein. Several computational methods have also been proposed for solving moving contact line problems without electric field, such as volume of fluid method [8–10], front tracking method [11], and level set method [12–15]. However, there is much less published work on contact line dynamics under the actuation of electric field, which was considered as one of the open problems in electrowetting [16]. In this paper, we present a dynamic contact line model under the actuation of electric field. We derive our moving contact line model from the energy dissipation point of view, by generalizing the approaches for the non-electric case [17].

A conceptual EWD set up is shown in Fig. 1, where a conducting drop surrounded by a dielectric fluid is placed on a hydrophobic dielectric layer, with an applied electric field between the drop and electrode under the dielectric layer. In the early electrowetting literature [1,2], it was widely accepted that the equilibrium interface of drop under electrowetting is a sphere shape, and the contact angle under electrowetting follows Lippmann-Young's relation [18]

$$\cos(\theta_{\mathrm{B}}) = \cos(\theta_0) + \mathrm{B}, \tag{1.1}$$

where $\mathrm{B} = \varepsilon_d \varepsilon_0 V^2 (2\gamma d)^{-1}$ is the electric Bond number, d is the height of the insulating dielectric layer, V is the applied voltage, θ_0 is the Young's angle which is the equilibrium contact angle without electric field, θ_{B} is the equilibrium contact angle, γ is the interfacial tension between the two fluids, ε_0 is the vacuum permittivity, ε_d is the dielectric constant of the dielectric layer. However, recent experiments and static electrowetting theory [19,20] show that the equilibrium interface of the drop under electrowetting takes up a non-spherical shape with an interface boundary layer near the contact lines. The Lippmann-Young's relation is only applicable to the apparent static contact angle

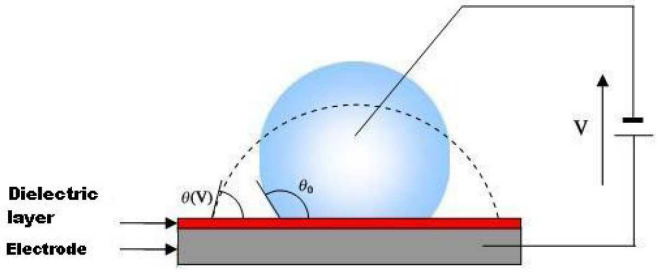


Figure 1: Electrowetting device.

https://doi.org/10.4208/cicp.200114.090316a Published online by Cambridge University Press

(macroscopic contact angle), while the local contact angle (microscopic contact angle) is determined by the Young's equation, unaffected by the electric field.

The main objective of this paper is to understand the contact line dynamics under electrowetting actuation. We introduce a mathematical model based on first principles and carry out numerical simulations using a level set method. Numerical results without imposing an electric field show that the method is first-order and results are consistent with those in the existing literature. Computing drop motion under electrowetting actuation, however, is a much more challenging problem. The main issue is that the electric field is singular at the moving contact lines. While the value of electric potential is bounded, its derivatives are not. The electric force on the drop surface is directly proportional to the electric field, which is unbounded at the contact lines. This suggest that some form of regularization is needed. In this paper, we tested a simple discretization method to compute the electric force at the drop surface without modifying the underlying contact line model. The rationale is that the discretization may provide the regularization needed and the results are mixed. On the one hand, our results agree with the experimentally observed maximum deformation while the applied electric field strength varies. On the other hand, after the maximum deformation has been reached, the singular electric field seems to induce numerical instability. This suggest that a follow up work is needed to address the effect of the singularity of the electric force at the contact point, which will be the subject of a future project.

The rest of the paper is organized as follows. In Section 2, we present the mathematical model and put the derivation of the model in Appendix A. Numerical method is given in Section 3. Section 4 gives numerical results for the two-phase contact line model without electric field. Section 5 shows the numerical results of our electrowetting two-phase flow model and comparison with the experiments. A brief conclusion and discussion of future directions is given in Section 6.

2 Mathematical model

We consider a mathematical model for a common experiment in electrowetting, where a perfect conducting water drop surrounded by silicone oil (dielectric fluid) is placed on the electrowetting device, as shown in Fig. 2, also see [19]. In the experiment, salts are added into the water drop so that the conductivity of the drop is high so that we can assume that the water drop is a perfect conductor, which is also a common assumption in the electrowetting literature [1,2]. Taking the axisymmetric property of the problem into account, the electric field potential Φ (scaled by V) can be modeled as following Laplace equation

$$\frac{1}{r}(r\varepsilon\Phi_r)_r+(\varepsilon\Phi)_z=0, \quad \text{in } \Omega_d\cup\Omega_+, \tag{2.1}$$

and $\Phi=0$ in Ω_-, where Ω_d is the insulating dielectric layer of the electrowetting device, Ω_- and Ω_+ are the domain occupied by water and silicone oil, respectively, $\varepsilon=\varepsilon_d$ in Ω_d

https://doi.org/10.4208/cicp.200114.090316a Published online by Cambridge University Press

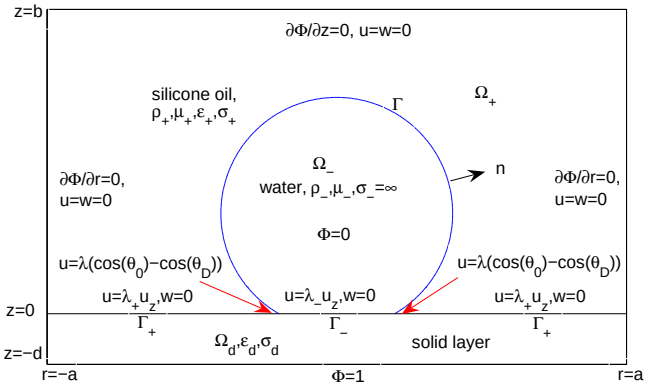


Figure 2: Axisymmetric domain.

and $\varepsilon=\varepsilon_+$ in Ω_+, here ε_d and ε_+ are the dielectric constants of the dielectric layer and silicone oil, respectively. $\Phi=1$ is the boundary condition at the lower boundary of the dielectric layer ($z=-d$), and $\Phi_{\vec{n}}=0$ is used on other boundaries ($z=b$,$r=-a$, and $r=a$), cf. Fig. 2. Finally the electric field is given by $\mathbf{E}=-\nabla\Phi$.

The conducting water drop and surrounding silicon oil are modeled as incompressible fluids and the equations of motion are (in the axisymmetric form)

$$\rho(\phi)\left(u_t+uu_r+wu_z\right)=-p_r+S^r, \tag{2.2}$$

$$\rho(\phi)\left(w_t+uw_r+ww_z\right)=-p_z+S^z, \tag{2.3}$$

$$\frac{1}{r}(ru)_r+w_z=0 \tag{2.4}$$

in $\Omega=\Omega_-\cup\Omega_+$, where

$$S^r=\frac{1}{\mathrm{Re}}\left(\frac{2}{r}(r\mu u_r)_r+\left(\mu\left(u_z+w_r\right)\right)_z-\frac{2\mu u}{r^2}\right)+\frac{\left(\kappa+\mathrm{B}\tau\eta|\mathbf{E}|_+^2\right)\phi_r}{\mathrm{ReCa}}\delta(\phi),$$

$$S^z=\frac{1}{\mathrm{Re}}\left(\frac{1}{r}\left(r\mu\left(u_z+w_r\right)\right)_r+\left(2\mu w_z\right)_z\right)+\frac{\left(\kappa+\mathrm{B}\tau\eta|\mathbf{E}|_+^2\right)\phi_z}{\mathrm{ReCa}}\delta(\phi).$$

Here u and w are velocity components in r and z directions, respectively, p is the pressure, κ is the curvature of interface, Γ is the interface of two fluids, $|\mathbf{E}|_+$ is the magnitude of electric field on the silicon oil side of the interface, ϕ is the level set function which takes positive values in Ω_+, and negative values in Ω_-. The Reynolds and capillary numbers are defined as

$$\mathrm{Re}=\frac{\rho_{ref}L_{ref}U_{ref}}{\mu_{ref}},\quad \mathrm{Ca}=\frac{U_{ref}\mu_{ref}}{\gamma},\quad \eta=\frac{\varepsilon_+}{\varepsilon_d}.$$

Finally, we have

$$\rho(\phi)=\rho_-+(\rho_+-\rho_-)H(\phi),\quad \mu(\phi)=\mu_-+(\mu_+-\mu_-)H(\phi),$$

https://doi.org/10.4208/cicp.200114.090316a Published online by Cambridge University Press

where $\rho_\pm$, and $\mu_\pm$ are densities and viscosities of the oil and water, scaled by its reference values ρ_{ref} and μ_{ref}, respectively.

On the solid boundary, we apply the slip condition away from the contact lines

$$u=\lambda_\pm u_z, \quad w=0, \tag{2.5}$$

where $\lambda_\pm$ is the slip length on solid boundary under domain $\Omega_\pm$. The boundary condition on the contact lines are

$$u=\lambda(\cos\theta_0-\cos\theta_D), \quad w=0, \tag{2.6}$$

where θ_D is the dynamic contact angle, θ_0 is Young's angle and λ is a nondimensional parameter. The no-slip condition $u=w=0$ is used on other boundaries. The detailed derivation of the above model equations and boundary conditions can be found in Appendix A.

3 Numerical method

3.1 Discretization

Following [21], we use a staggered grid shown in Fig. 3, the velocity components u and w are stored on the face of the cells, the values of pressure p is stored at the center of each cell while the level set function ϕ is stored at the vertex of each cell. Since the computational domain $[a,b]\times[c,d]$ is a rectangle, we use uniform mesh $h=\Delta r=\Delta z$, $r_{i-\frac{1}{2}}$ is the i-th point in r direction, $i=1,\cdots,M,M+1$, where $Mh=b-a$, and $z_{j-\frac{1}{2}}$ is the j-th point in z direction, $j=1,\cdots,N,N+1$, where $Nh=d-c$. The discretization is done as follows

$$\begin{aligned}
&\phi^n_{i-\frac{1}{2},j-\frac{1}{2}}=\phi(r_{i-\frac{1}{2}},z_{j-\frac{1}{2}},t_n), \quad \phi^n_{i+\frac{1}{2},j-\frac{1}{2}}=\phi(r_{i+\frac{1}{2}},z_{j-\frac{1}{2}},t_n),\\
&\phi^n_{i-\frac{1}{2},j+\frac{1}{2}}=\phi(r_{i-\frac{1}{2}},z_{j+\frac{1}{2}},t_n), \quad \phi^n_{i+\frac{1}{2},j+\frac{1}{2}}=\phi(r_{i+\frac{1}{2}},z_{j+\frac{1}{2}},t_n),\\
&\Phi^n_{i-\frac{1}{2},j-\frac{1}{2}}=\Phi(r_{i-\frac{1}{2}},z_{j-\frac{1}{2}},t_n), \quad \Phi^n_{i+\frac{1}{2},j-\frac{1}{2}}=\Phi(r_{i+\frac{1}{2}},z_{j-\frac{1}{2}},t_n),\\
&\Phi^n_{i-\frac{1}{2},j+\frac{1}{2}}=\Phi(r_{i-\frac{1}{2}},z_{j+\frac{1}{2}},t_n), \quad \Phi^n_{i+\frac{1}{2},j+\frac{1}{2}}=\Phi(r_{i+\frac{1}{2}},z_{j+\frac{1}{2}},t_n),\\
&u_{i-\frac{1}{2},j}=u(r_{i-\frac{1}{2}},z_j), \qquad u_{i+\frac{1}{2},j}=u(r_{i+\frac{1}{2}},z_j),\\
&v_{i,j-\frac{1}{2}}=v(r_i,z_{j-\frac{1}{2}}), \qquad v_{i,j+\frac{1}{2}}=v(r_i,z_{j+\frac{1}{2}}),\\
&p^n_{i,j}=p(r_i,z_j,t_n).
\end{aligned}$$

Here $r_i=r_{i-\frac{1}{2}}+h/2$ and $z_j=z_{j-\frac{1}{2}}+h/2$ for $i=1,2,\cdots,M$ and $j=1,2,\cdots,N$.

3.2 Algorithm

Initially, the level set function ϕ is defined as a signed distance function which takes negative values in Ω_- and positive values in Ω_+, and zeros on the interface Γ. Assuming

https://doi.org/10.4208/cicp.200114.090316a Published online by Cambridge University Press

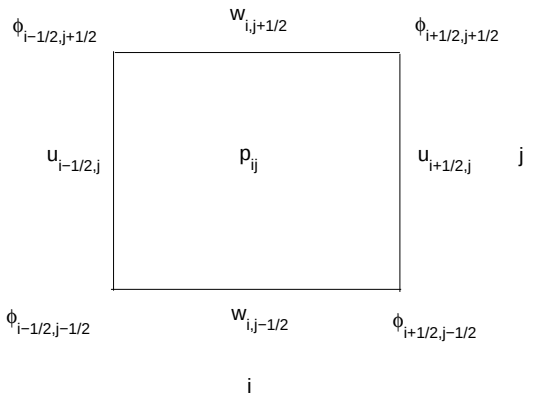


Figure 3: Staggered grid used for the discretization.

that $p^n_{i,j}$, $u^n_{i+\frac{1}{2},j}$, $w^n_{i,j+\frac{1}{2}}$, $\phi^n_{i+\frac{1}{2},j-\frac{1}{2}}$ at time level n is known for each cell (i,j), we have the following steps to compute the corresponding variables at time level $n+1$.

1. A fictitious layer is defined for the velocity component u on $z=z_0$, where $z_0 = z_{\frac{1}{2}} - h/2$. By linear interpolation, we find the zero level set on the solid boundary i.e., the position of the two contact points r_L and r_R, where r_L is the left contact point while r_R is the right contact point. One side second-order finite difference method is used to calculate ϕ_z on the solid boundary as follows

$$(\phi_z)_{i+\frac{1}{2},\frac{1}{2}} = \frac{-3\phi_{i+\frac{1}{2},\frac{1}{2}} + 4\phi_{i+\frac{1}{2},\frac{3}{2}} - \phi_{i+\frac{1}{2},\frac{5}{2}}}{2h}, \tag{3.1}$$

and a second-order central difference method is used to calculate ϕ_r. Using linear interpolation, we find the norm vector $\vec{n} = (n_r, n_z)$ on the solid boundary at each level set stored point at the contact point r_L and r_R using

$$n_r = \frac{\phi_r}{\sqrt{\phi_r^2+\phi_z^2}}, \quad n_z = \frac{\phi_z}{\sqrt{\phi_r^2+\phi_z^2}}.$$

Since $\vec{t} = (n_z, -n_r)$, we could compute the dynamic contact angle at right contact point through

$$\theta_R = \arccos(\vec{t}_R \cdot \vec{e}_1), \tag{3.2}$$

where $\vec{e_1} = (1,0)$. The boundary condition (2.6) on the contact points requires

$$u_R = \lambda(\cos\theta_0 - \cos\theta_R), \tag{3.3}$$

where u_R is the velocity component of right contact point in the r direction. In order to implement the velocity boundary condition (3.3) efficiently, we use a similar

https://doi.org/10.4208/cicp.200114.090316a Published online by Cambridge University Press

approach in [22], we assume that there is a velocity transition in the contact line region from the right contact point r_R to the regions outside the right contact region, a smooth version of the velocity in the right contact line region is given by

$$u_t = \lambda(\cos\theta_0 - \cos\theta_R)e^{-\left(\frac{r-r_R}{r_w}\right)^2},$$

where r_w is the width of contact line region, and r_w is $\mathcal{O}(h)$ [7, 22]. A similar approach is used in the left transit contact line region. Here we point out that [22] solves the contact line motion of a one-phase flow equations without electric field by an immersed interface method, however, our model is a two-phase flow model, we need to solve the two-phase Navier-Stokes equations, where the algorithm is presented as follows.

For the contact line regions, the velocity on the fictitious layer is prescribed as

$$u^n_{i+\frac{1}{2},0} = 2u_t - u^n_{i+\frac{1}{2},1}, \tag{3.4}$$

and for other regions, the velocity on the fictitious layer is prescribed as

$$u^n_{i+\frac{1}{2},0} = \frac{\nu - \frac{h}{2}}{\nu + \frac{h}{2}} u^n_{i+\frac{1}{2},1}, \tag{3.5}$$

where $\nu = \lambda_+$ or λ_- depending on which phase it locates. In addition, fictitious layers are also defined for the other boundaries, and the velocities values on these fictitious layers are assigned based on the no-slip conditions.

2. Use the above prescribed velocities to update the velocities in the computational domain $u_{i+\frac{1}{2},j}$ for $i = 0,1,2,\cdots,M$ and $j = 1,2,\cdots,N$ and $w_{i,j+\frac{1}{2}}$ for $i = 1,2,\cdots,M$ and $j = 0,1,2,\cdots,N$ by solving the fluid equations. A modified MAC projection method is proposed for the fluid solver as follows.

   (a) Prediction step.

$$\rho_{i+\frac{1}{2},j}\left(\frac{u^*_{i+\frac{1}{2},j} - u^n_{i+\frac{1}{2},j}}{\Delta t}\right) = (-uu_r - wu_z + S^r)^n_{i+\frac{1}{2},j}, \tag{3.6}$$

$$\rho_{i,j+\frac{1}{2}}\left(\frac{w^*_{i,j+\frac{1}{2}} - w^n_{i,j+\frac{1}{2}}}{\Delta t}\right) = (-uw_r - ww_z + S^z)^n_{i,j+\frac{1}{2}}, \tag{3.7}$$

where

$$\rho_{i+\frac{1}{2},j} = \rho_1 + (\rho_2 - \rho_1)H\left(\frac{\phi_{i+\frac{1}{2},j-\frac{1}{2}} + \phi_{i+\frac{1}{2},j+\frac{1}{2}}}{2}\right), \tag{3.8}$$

$$\rho_{i,j+\frac{1}{2}} = \rho_1 + (\rho_2 - \rho_1)H\left(\frac{\phi_{i-\frac{1}{2},j+\frac{1}{2}} + \phi_{i+\frac{1}{2},j+\frac{1}{2}}}{2}\right), \tag{3.9}$$

https://doi.org/10.4208/cicp.200114.090316a Published online by Cambridge University Press

$$(S^r)^n_{i+\frac{1}{2},j}=\frac{(S^r)^n_{i+\frac{1}{2},j-\frac{1}{2}}+(S^r)^n_{i+\frac{1}{2},j+\frac{1}{2}}}{2}, \tag{3.10}$$

$$(S^z)^n_{i,j+\frac{1}{2}}=\frac{(S^z)^n_{i-\frac{1}{2},j+\frac{1}{2}}+(S^z)^n_{i+\frac{1}{2},j+\frac{1}{2}}}{2}, \tag{3.11}$$

and S^r and S^z are the forcing terms on the right hand side of the equations (2.2) and (2.3), respectively. $H(\cdot)$ is the Heaviside function.

The delta function is regularized as

$$\delta_\epsilon(\phi)=\begin{cases} 0, & \text{if } |\phi|>\varepsilon, \\ \frac{1}{2\varepsilon}+\frac{1}{2\varepsilon}\cos\left(\frac{\pi\phi}{\varepsilon}\right), & \text{if } -\varepsilon\le\phi\le\varepsilon, \end{cases} \tag{3.12}$$

where ε is a small positive number, which is set to be $1.5h$ in our computation. The calculation of electric force is crucial for this problem, we first need to solve the electric potential equation (2.1), where a standard method is used. We set $\Phi_{i+\frac{1}{2},j-\frac{1}{2}}=0$ for all grid points $(r_{i+\frac{1}{2}},z_{j-\frac{1}{2}})\in\Omega_-$, and use standard five points central difference method for the electric potential equation (2.1) in Ω_+ and Ω_d. Then we set $\vec{E}=0$ in Ω_- and use the standard central difference method to calculate electric field $\vec{E}=-\nabla\Phi$ from Eq. (2.1) in Ω_+. However, the electric force quantity is not continuous across the drop interface. Since the level set method is a fully Eulerian method and only the force acting on the "+" side of the drop interface is useful for our problem. Numerically, when using the discretized the delta function (3.12) for (2.2)-(2.3), the electric force acting on the drop "+" side of the interface needs to be spread into a neighborhood of the interface smoothly so that the quantity acting on the interface is calculated correctly[†]. After obtaining electric field, we keep the values $\vec{E}$ in Ω_+ unchanged, and extend the values $\vec{E}$ from Ω_+ to a neighbourhood of drop interface "-" side in Ω_- using an simple artificial averaging method in this paper. The details are explained in the following paragraph.

We find the grid points located at a neighbourhood of the drop interface "-" side in Ω_-, i.e. grid point $(r_{i+\frac{1}{2}},z_{j-\frac{1}{2}})$ that satisfies $-\epsilon\le\phi_{i+\frac{1}{2},j-\frac{1}{2}}\le 0$, where ϵ is set to be 3h. For every such grid point, we assign the new value at grid point $(r_{i+\frac{1}{2}},z_{j-\frac{1}{2}})$ as

$$\vec{E}_{i+\frac{1}{2},j-\frac{1}{2}}=\frac{\sum_{s=1}^{5}\vec{E}_{i+i_s+\frac{1}{2},j+j_s-\frac{1}{2}}}{5},$$

[†]This requirement can be seen from the force term that appeared in the Navier-Stokes equation of the level set formulations (2.2) and (2.3), numerically, the force acting on the drop "+" side of interface needs to be spread into the Eulerian points in a neighbourhood of the interface through a regularized delta function (3.12), thus force quantities at Eulerian points on both sides of the interface are used in the numerical calculation. Following [24–26], these quantities need to be smooth in a neighbourhood of the interface in order to calculate the electric force acting on the interface correctly.

https://doi.org/10.4208/cicp.200114.090316a Published online by Cambridge University Press

where $(i_s,j_s)\in\{(0,0),(1,0),(0,1),(-1,0),(0,-1)\}$. We perform this averaging process several times in the neighbourhood of interface at the "-" side in order to extend the electric field continuously from the "+" side to the "-" side.

The detail discretization of the convection term and viscous term in the first prediction equation (3.6) is given as follows

$$
\begin{aligned}
&(uu_r)_{i+\frac{1}{2},j}=u_{i+\frac{1}{2},j}\frac{u_{i+\frac{3}{2},j}-u_{i-\frac{1}{2},j}}{2\Delta r},\\
&(wu_z)_{i+\frac{1}{2},j}=w_{i+\frac{1}{2},j}\frac{u_{i+\frac{1}{2},j+1}-u_{i+\frac{1}{2},j-1}}{2\Delta z},\\
&w_{i+\frac{1}{2},j}=\frac{1}{4}(w_{i,j+\frac{1}{2}}+w_{i,j-\frac{1}{2}}+w_{i+1,j+\frac{1}{2}}+w_{i+1,j-\frac{1}{2}}),\\
&\left(\frac{(r\mu u_r)_r}{r}\right)_{i+\frac{1}{2},j}=\frac{r_{i+1,j}\mu_{i+1,j}(u_{i+\frac{3}{2},j}-u_{i+\frac{1}{2},j})-r_{i,j}\mu_{i,j}(u_{i+\frac{1}{2},j}-u_{i-\frac{1}{2},j})}{r_{i+\frac{1}{2},j}(\Delta r)^2},\\
&\mu_{i,j}=\mu_1+(\mu_2-\mu_1)H\left(\frac{\phi_{i-\frac{1}{2},j-\frac{1}{2}}+\phi_{i-\frac{1}{2},j+\frac{1}{2}}+\phi_{i+\frac{1}{2},j-\frac{1}{2}}+\phi_{i+\frac{1}{2},j+\frac{1}{2}}}{4}\right),\\
&((\mu u_z)_z)_{i+\frac{1}{2},j}=\frac{\mu_{i+\frac{1}{2},j+\frac{1}{2}}(u_{i+\frac{1}{2},j+1}-u_{i+\frac{1}{2},j})-\mu_{i+\frac{1}{2},j-\frac{1}{2}}(u_{i+\frac{1}{2},j}-u_{i+\frac{1}{2},j-1})}{(\Delta z)^2},\\
&((\mu w_r)_z)_{i+\frac{1}{2},j}=\frac{\mu_{i+\frac{1}{2},j+\frac{1}{2}}(w_{i+1,j+\frac{1}{2}}-w_{i,j+\frac{1}{2}})-\mu_{i+\frac{1}{2},j-\frac{1}{2}}(w_{i+1,j-\frac{1}{2}}-w_{i,j-\frac{1}{2}})}{\Delta r\Delta z},\\
&\mu_{i+\frac{1}{2},j+\frac{1}{2}}=\mu_1+(\mu_2-\mu_1)H\left(\phi_{i+\frac{1}{2},j+\frac{1}{2}}\right),\\
&\left(-\frac{\mu u}{r^2}\right)_{i+\frac{1}{2},j}=-\frac{\mu_{i+\frac{1}{2},j}u_{i+\frac{1}{2},j}}{r^2_{i+\frac{1}{2},j}}.
\end{aligned}
$$

A similar approach is used for Eq. (3.7).

(b) Projection step.

$$u^{n+1}_{i+\frac{1}{2},j}=u^*_{i+\frac{1}{2},j}-\frac{\Delta t}{\Delta r}\frac{p^{n+1}_{i+1,j}-p^{n+1}_{i,j}}{\rho_{i+\frac{1}{2},j}},\tag{3.13}$$

$$w^{n+1}_{i,j+\frac{1}{2}}=w^*_{i,j+\frac{1}{2}}-\frac{\Delta t}{\Delta z}\frac{p^{n+1}_{i,j+1}-p^{n+1}_{i,j}}{\rho_{i,j+\frac{1}{2}}},\tag{3.14}$$

where $u^{n+1}_{i+\frac{1}{2},j}$ and $w^{n+1}_{i,j+\frac{1}{2}}$ subject to the incompressible condition on each cell (i,j)

$$\frac{r_{i+\frac{1}{2}}u^{n+1}_{i+\frac{1}{2},j}-r_{i-\frac{1}{2}}u^{n+1}_{i-\frac{1}{2},j}}{r_i\Delta r}+\frac{w^{n+1}_{i,j+\frac{1}{2}}-w^{n+1}_{i,j-\frac{1}{2}}}{\Delta z}=0.\tag{3.15}$$

https://doi.org/10.4208/cicp.200114.090316a Published online by Cambridge University Press

Substituting (3.13) and (3.14) into (3.15) yields the following poisson equation for pressure p^{n+1}

$$\begin{aligned}&\frac{\Delta t}{(\Delta r)^2}\left(\frac{r_{i+\frac{1}{2}}(p^{n+1}_{i+1,j}-p^{n+1}_{i,j})}{r_i\rho_{i+\frac{1}{2},j}}-\frac{r_{i-\frac{1}{2}}(p^{n+1}_{i,j}-p^{n+1}_{i-1,j})}{r_i\rho_{i-\frac{1}{2},j}}\right)\\&+\frac{\Delta t}{(\Delta z)^2}\left(\frac{p^{n+1}_{i,j+1}-p^{n+1}_{i,j}}{\rho_{i,j+\frac{1}{2}}}-\frac{p^{n+1}_{i,j}-p^{n+1}_{i,j-1}}{\rho_{i,j-\frac{1}{2}}}\right)\\=&\frac{r_{i+\frac{1}{2}}u^*_{i+\frac{1}{2},j}-r_{i-\frac{1}{2}}u^*_{i-\frac{1}{2},j}}{r_i\Delta r}+\frac{w^*_{i,j+\frac{1}{2}}-w^*_{i,j-\frac{1}{2}}}{\Delta z}.\end{aligned}\tag{3.16}$$

3. Update the level set function from $\phi^n_{i+\frac{1}{2},j+\frac{1}{2}}$ to $\phi^{n+1}_{i+\frac{1}{2},j+\frac{1}{2}}$ using the velocity at time level n by solving the following transportation equation

$$\phi_t+\vec{u}\cdot\nabla\phi=0.\tag{3.17}$$

For spatial discretization, we do the following. A first-order upwind scheme is used for the first three layers of grid points near the boundary while a 5th-order upwind HJWENO scheme is used for other internal grid points. For time integration, a 3rd-order Runge-Kutta TVD scheme is used and

$$\begin{aligned}u^n_{i+\frac{1}{2},j+\frac{1}{2}}&=\frac{u^n_{i+\frac{1}{2},j}+u^n_{i+\frac{1}{2},j+1}}{2},\\w^n_{i+\frac{1}{2},j+\frac{1}{2}}&=\frac{w^n_{i,j+\frac{1}{2}}+w^n_{i+1,j+\frac{1}{2}}}{2}\end{aligned}\tag{3.18}$$

is used for evaluating the velocity on the cell vertices.

4. Reinitialize the level set function by solving the following equation

$$\phi_\tau+\frac{\phi_0}{\sqrt{\phi_0^2+h^2}}(|\nabla\phi|-1)=0\tag{3.19}$$

until the "steady state" is reached, where ϕ_0 represents the level set function before reinitialization. We use a Godunov scheme for the above equation [27, 28]. For spatial discretization, we use the following method, for the first three layers of grid points near the boundary, a first-order scheme is used, while for other internal grid points, we use a fifth order HJWENO scheme, and a forward Euler scheme is used for time integration.

When numerically solving the level set equations (3.17) and (3.19), we apply the following boundary conditions outside fictitious layer $z_{-\frac{1}{2}}=z_{\frac{1}{2}}-h$ so that the spatial derivatives $\phi^{\pm}_z=0$ on the horizontal boundaries are approximated as

$$\phi_{i+\frac{1}{2},-\frac{1}{2}}=2\phi_{i+\frac{1}{2},\frac{1}{2}}-\phi_{i+\frac{1}{2},\frac{3}{2}}.\tag{3.20}$$

https://doi.org/10.4208/cicp.200114.090316a Published online by Cambridge University Press

Similar treatment is used for approximating $\phi_r^{\pm}=0$ on the vertical boundaries. We should point out that the boundary condition (3.20) implies that the angle that the iso-surfaces of ϕ intersect with the solid boundary is 90^o, which is generally inconsistent with the contact angle of drop interface, however, in this paper we simply assign the values of ϕ on the fictitious layer by using (3.20) so that the first-order upwind Godunov scheme can be used for the advection (3.17) and the reinitialization (3.19) on the entire solid boundary, respectively. Note that our treatment for reinitialization here is different from that in [29] where two different equations are used for reinitialization on the boundary based on the characteristic of Eq. (3.19). Since mass is not strictly conserved due to the numerical discretization of level set equations (3.17) and (3.19), we use a constrained approach as in [30] to minimize its effect in our implementation.

4 Numerical results without the electric field

In this section, we present several numerical results for the two-phase flow model without electric field to demonstrate the applicability of our numerical scheme. Unless otherwise indicated, throughout this section, we use a two-dimensional computational domain $[0,2]\times[0,1]$ where a half circular drop with radius 0.4 is initially attached at the bottom of the domain i.e. $z=0$. The initial contact angle is $\pi/2$, the static contact angle is $\pi/4$, the initial velocity is set to be zero, and $\mathrm{Re}=6.731$, $\mathrm{Ca}=6.74\times10^{-2}$, $\lambda_+=\lambda_-=h/2$, $\lambda=1$, $r_w=3h$, and $\varepsilon=1.5h$.

4.1 Convergence analysis

4.1.1 Convergence study for the velocity field

We first carry out a convergence study of our numerical method presented above. Our test are based on four different cases listed in Table 1, in each case, we compute with varying Cartesian mesh $h=2^{-i}$, $i=4,5,6,7$. For each h, the solutions are computed up to time $T=0.5$ with time step size $\Delta t=8h^2/5$.

Table 1: Parameter values for four test cases.

	ρ_1	μ_1	ρ_2	μ_2
Case I	1	1	1	1
Case II	1	1	10	1
Case III	1	1	1	0.1
Case IV	1	1	10	0.1

Since the analytical solution is not available, we use the results from the finest mesh and finest time step as our reference solution, and compute L_2 error between the reference solution and the solutions obtained on the coarse grid. Tables 2-5 show the results of

https://doi.org/10.4208/cicp.200114.090316a Published online by Cambridge University Press

Table 2: Convergence analysis of the velocity for case I.

h	$\|\|u-u_{ref}\|\|_2$	ratio	$\|\|v-v_{ref}\|\|_2$	ratio
2^{-4}	2.22155e-2	-	1.3046e-2	-
2^{-5}	1.0171e-2	2.1782	6.9456e-3	1.8782
2^{-6}	4.5395e-3	2.2406	3.0392e-3	2.2854
2^{-7}	1.6187e-3	2.8044	1.2084e-3	2.5151

Table 3: Convergence analysis of the velocity for case II.

h	$\|\|u-u_{ref}\|\|_2$	ratio	$\|\|v-v_{ref}\|\|_2$	ratio
2^{-4}	2.4889e-2	-	1.4801e-2	-
2^{-5}	1.2868e-2	1.9341	6.6817e-3	2.2152
2^{-6}	5.5122e-3	2.3345	3.2835e-3	2.0349
2^{-7}	2.0245e-3	2.7227	1.4158e-3	2.3192

Table 4: Convergence analysis of the velocity for case III.

h	$\|\|u-u_{ref}\|\|_2$	ratio	$\|\|v-v_{ref}\|\|_2$	ratio
2^{-4}	1.597e-2	-	1.4338e-2	-
2^{-5}	9.0271e-3	1.7691	6.3518e-3	2.2574
2^{-6}	4.0115e-3	2.2503	2.7226e-3	2.3330
2^{-7}	1.4606e-3	2.7465	1.0262e-3	2.6531

Table 5: Convergence analysis of the velocity for case IV.

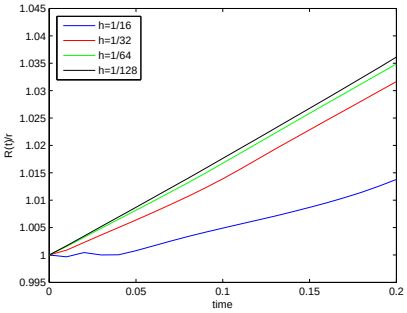
h	$\|\|u-u_{ref}\|\|_2$	ratio	$\|\|v-v_{ref}\|\|_2$	ratio
2^{-4}	3.7046e-2	-	3.6149e-2	-
2^{-5}	1.8409e-2	2.0124	1.6043	2.2533
2^{-6}	7.7767e-3	2.3672	6.9722e-3	2.3010
2^{-7}	2.509e-3	3.0995	2.3945e-3	2.9118

velocity. One can see that the ratio between two consecutive errors of each velocity component is between 2 and 3, which indicates that the method is first-order accurate [31].

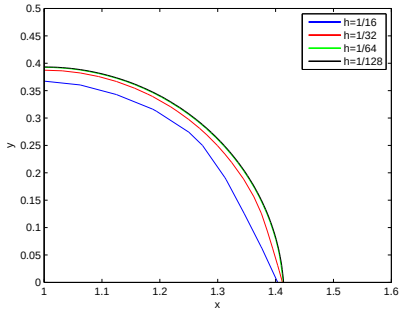
4.1.2 Parametric study

We now investigate the effect of parameter λ and $\lambda_{\pm}$ on the drop interface shape. We consider the drop spreading problem described in Section 4, where the density and viscosity values from Case I are used. In addition, λ is taken to be 0.1 or 1, and $\lambda_{\pm}$ varies among 0, 0.001 and 0.1. Other parameters are the same as described in the beginning of Section 4 with the final computational time set as $T=0.2$. The time step is set to be $\Delta t=10^{-4}$, and mesh size varies among $h=2^{-4},2^{-5},2^{-6}$, and 2^{-7}. In Fig. 4, the evolution

https://doi.org/10.4208/cicp.200114.090316a Published online by Cambridge University Press

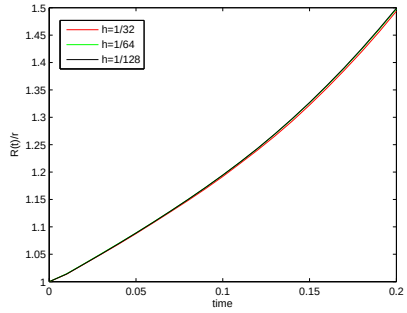


(a) Evolution of $R(t)/r$.

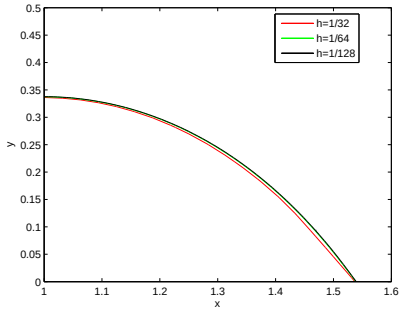


(b) Drop shapes (half) at $T=0.2$, the contact line moves from left to right.

Figure 4: Convergence study with different mesh resolutions for $\lambda=0.1$, $\lambda_{\pm}=0$.



(a) Evolution of $R(t)/r$.



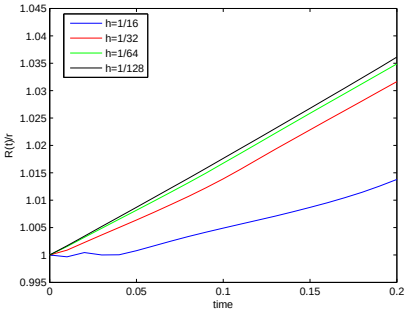
(b) Drop shapes (half) at $T=0.2$, the contact line moves from left to right.

Figure 5: Convergence study with different mesh resolutions for $\lambda=1$, $\lambda_{\pm}=0$.

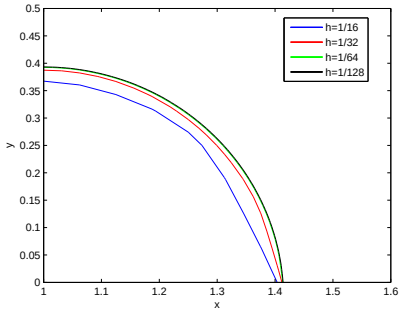
of $R(t)/r$ and drop shapes at $T=0.2$ with different mesh spacing with $\lambda=0.1$, $\lambda_{\pm}=0$, Fig. 5 gives the evolution of $\frac{R(t)}{r}$ and drop shapes at $T=0.2$ with different mesh spacing with $\lambda=1$, $\lambda_{\pm}=0$, Fig. 6 gives the evolution of $\frac{R(t)}{r}$ and drop shapes at $T=0.2$ are plotted for $\lambda=0.1$, $\lambda_{\pm}=0.001$. Similar plots are given in Fig. 7 for $\lambda=1$, $\lambda_{\pm}=0.001$, in Fig. 8 for $\lambda=0.1$, $\lambda_{\pm}=0.1$, and in Fig. 9 for $\lambda=1$, $\lambda_{\pm}=0.1$, where r is the initial radius of the drop, and $R(t)$ is the instantaneous drop radius at time t.

On the one hand, by comparing Figs. 4-5, Figs. 6-7, and Figs. 8-9 in pairs, we observe that when $\lambda_{\pm}$ is fixed, the drop interface seems to approach to an asymptotic shape when mesh is refined. Furthermore, the convergence is faster for large λ values since the drop evolves faster. On the other hand, by comparing Figs. 4, 6, and 8 with Figs. 5, 7, and 9, it can be seen that the evolution of interface location is not affected by changing parameter $\lambda_{\pm}$. This is due to the fact that the Navier slip boundary condition (2.5) is only applied on the solid boundary away from contact line. Thus the slip velocity on the solid boundary

https://doi.org/10.4208/cicp.200114.090316a Published online by Cambridge University Press

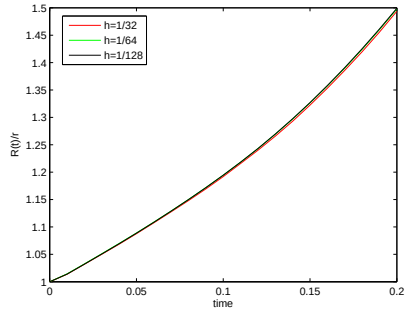


(a) Evolution of $R(t)/r$.

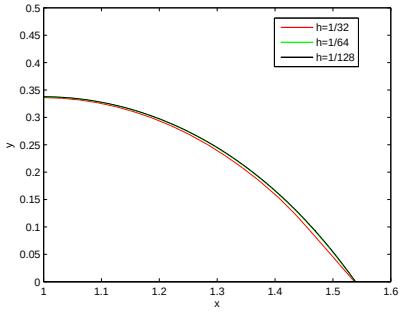


(b) Drop shapes (half) at $T=0.2$, the contact line moves from left to right.

Figure 6: Convergence study with different mesh resolutions for $\lambda=0.1$, $\lambda_{\pm}=0.001$.



(a) Evolution of $R(t)/r$.



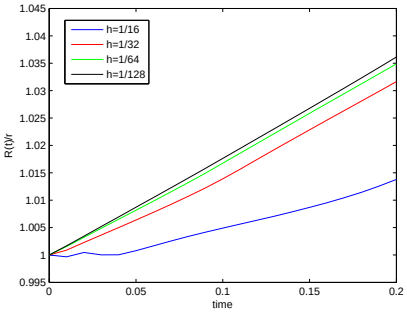
(b) Drop shapes (half) at $T=0.2$, the contact line moves from left to right.

Figure 7: Convergence study with different mesh resolutions for $\lambda=1$, $\lambda_{\pm}=0.001$.

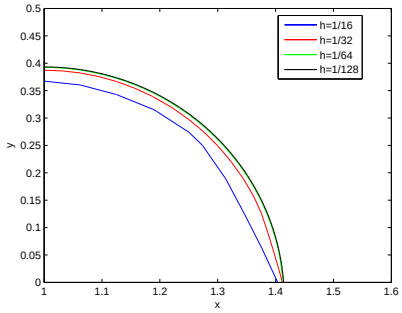
away from the contact line does not affect the motion of contact line.

We note that the mathematical derivation of our contact line model (2.5)-(2.6) follows that in [7, 17], while our numerical treatment of these conditions is different from that in [7, 17]. In [7, 17], the contact angle condition (2.6) is added to the Navier slip condition (2.5) as a singular force, and the resulting combined condition is solved on the entire solid boundary. Our numerical implementation of the contact line conditions (2.5)-(2.6) is similar to the method in [22]. Our method is also different from [9, 13–15], where the Navier slip boundary condition is applied on the entire solid boundary and the slip length must be resolved so that the convergent results can be obtained. In our model, Navier slip boundary conditions are only applied away from the contact lines, parameters $\lambda_{\pm}$ has no direct impact for the motion of contact line, while parameter λ is the most important factor that determines the motion of contact line. Numerically, our choice of $r_w=3h>\varepsilon=1.5h$ is used to minimize the impact of $\lambda_{\pm}$ on the motion of contact lines.

https://doi.org/10.4208/cicp.200114.090316a Published online by Cambridge University Press

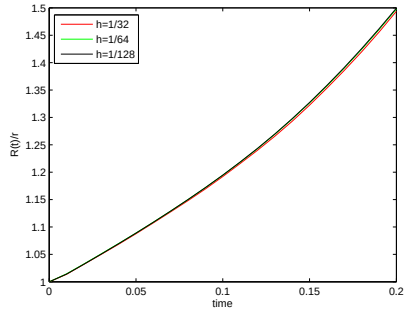


(a) Evolution of $R(t)/r$.

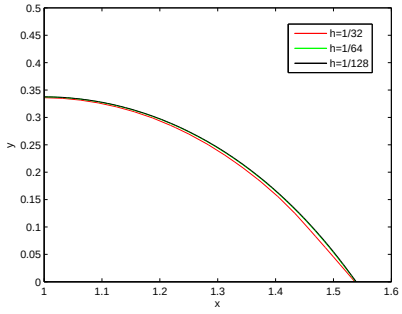


(b) Drop shapes (half) at $T=0.2$, the contact line moves from left to right.

Figure 8: Convergence study with different mesh resolutions for $\lambda=0.1$, $\lambda_{\pm}=0.1$.



(a) Evolution of $R(t)/r$.



(b) Drop shapes (half) at $T=0.2$, the contact line moves from left to right.

Figure 9: Convergence study with different mesh resolutions for $\lambda=1$, $\lambda_{\pm}=0.1$.

4.2 Drop spreading and recoiling

Here we perform numerical study for a drop spreading and recoiling process using a similar example from [22]. We use the parameters described in the beginning of this section, and the density and viscosity values are set to be same as in case I in Section 4.1 with $h=2^{-6}$. A few snapshots of the drop shape are shown in Fig. 10. The evolution of dynamic contact angle and the speed of the left contact point are given in Fig. 11. As we can see that the dynamic contact angle converges to the static contact angle and contact point speed approaches to zero. In the second case, we increase the static contact angle from $\pi/4$ to $3\pi/4$. The recoiling process is given in Fig. 12 and Fig. 13 gives the evolution of dynamic contact angle and the speed of the left contact point. These results are consistent with those in [22] and [8].

https://doi.org/10.4208/cicp.200114.090316a Published online by Cambridge University Press

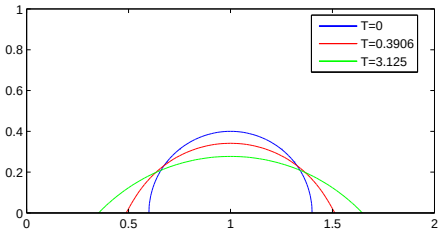


Figure 10: Snapshot for a drop motion with static contact angle $\frac{\pi}{4}$.

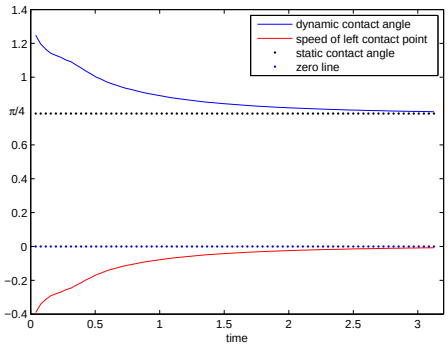


Figure 11: Evolution of dynamic contact angle and speed of the left contact point.

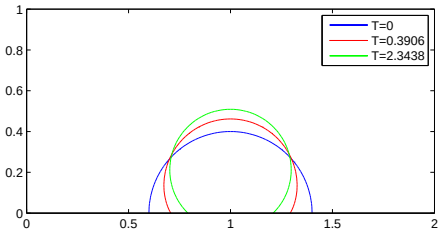


Figure 12: Snapshot for a drop motion with static contact angle $\frac{3\pi}{4}$.

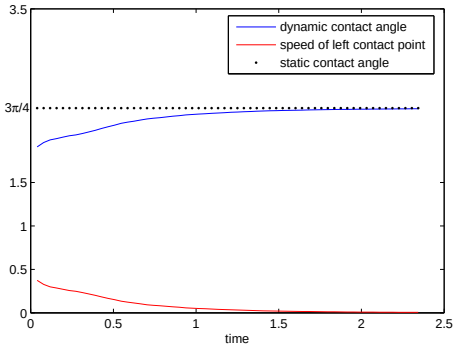


Figure 13: Evolution of dynamic contact angle and speed of the left contact point.

5 Results for the electrowetting contact line model

In this section, we present our numerical results and compare them with the experimental observations in [19]. The dimensionless axisymmetric computational domain for fluid is $\Omega=\{(r,z),0\le r\le 2.1,0\le z\le 2.1\}$, while the domain for electric field is $\Omega_*=\{(r,z),0\le r\le 2.1,-0.15\le z\le 2.1\}$. We use a uniform mesh 140×140 for the fluid equations and a uniform mesh 140×150 for electric potential equation. The physical parameters are listed in Table 6, corresponding to the experiments done in [19]. Based on the experimental observations, we choose $U_{ref}=10^{-3}$ m/s as the characteristic velocity, $L_{ref}=10^{-3}$ m as the characteristic length scale, $\rho_{ref}=\rho_-$ as the characteristic density, $\mu_{ref}=\mu_-$ as the characteristic viscosity, from which we obtain $\mathrm{Re}=0.8795$, and $\mathrm{Ca}=2.9921\times 10^{-5}$. We

https://doi.org/10.4208/cicp.200114.090316a Published online by Cambridge University Press

Table 6: Physical dimensional parameter values used in the computation, corresponding to the experiment done in [19].

Physical parameters	Values	Units
Teflon layer height d	150	μm
Dynamic viscosity of water μ_-	0.001137	Pa· s
Density of water ρ_-	1000	kg/m^3
Dynamic viscosity of silicone oil μ_+	0.005	Pa· s
Density of silicone oil ρ_+	800	kg/m^3
Interfacial tension between water and silicone oil γ	38	mJ/m^2
Dielectric constant of silicon oil ε_+	2. 5	
Dielectric constant of Teflon layer ε_d	2. 1	
Droplet contact angle in silicon oil at zero voltage θ_0	170	$^\circ$
Radius of water drop	0.75	mm

use $\lambda_+ = \lambda_- = h/2$, $r_w = 3h$, and $\lambda = 1$[‡]. And other non-dimensional parameters can be estimated using the values in Table 6.

Our numerical results show that the interface near the contact line region deviates from a spherical cap, which is consistent with equilibrium shape observed in the experiments [19]. Since the apparent contact angle (macroscopic contact angle) is not well defined, we compute its value by fitting a circular arc of the original interface over the interface boundary layer and extend the circular arc to the solid boundary as in [9], cf. Fig. 14. We assume that 2d is the height of interface boundary layer, since the height of boundary

[‡]We tried several other set of parameters, different parameters will give different time scales, larger λ gives smaller the time scale to reach "steady state" while smaller λ produces larger time scale to reach "steady state", however, results are qualitatively similar.

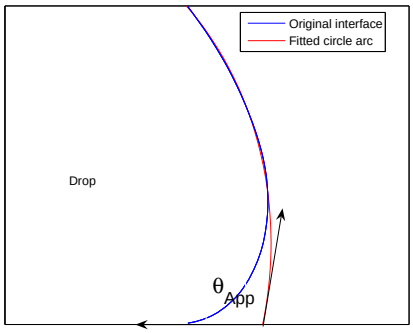


Figure 14: Fitting original interface over a boundary layer with a circular arc and extending to the solid boundary to calculate the apparent contact angle as in [9]. (The angle composed by the two arrows is the apparent contact angle in the figure.)

https://doi.org/10.4208/cicp.200114.090316a Published online by Cambridge University Press

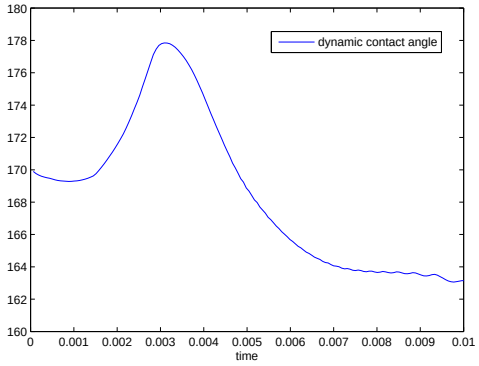


Figure 15: Evolution of dynamic contact angle

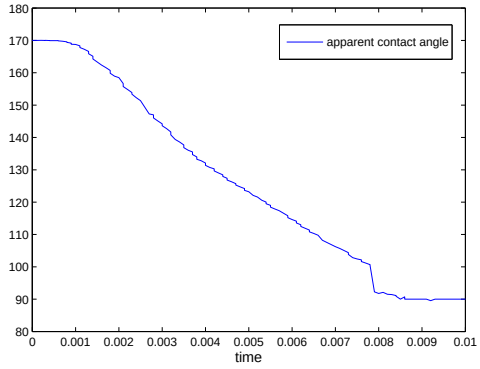


Figure 16: Evolution of apparent contact angle.

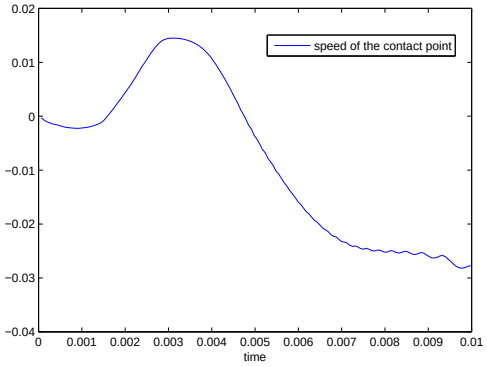


Figure 17: Speed of the contact point with respect to time

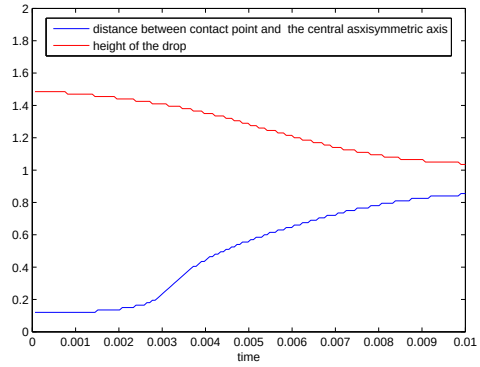


Figure 18: Evolution of two distances, which measure the drop deformation.

layer is $\mathcal{O}(\mathrm{d})$ [19]. The dynamic contact angle (microscopic contact angle) is calculated according to (3.2). In Fig. 15, the evolution of the dynamic contact angle is plotted while in Fig. 16, the evolution of the apparent contact angle is plotted. Fig. 17 gives the speed of contact point, where contact point speed is calculated using (3.3). Fig. 18 gives the evolution of the drop height and the distance between the contact point and the central axisymmetric axis.

We now take the solutions at the end of these computations and treat them as our "steady state" solutions and compare them with experimental observations. The comparison between our "steady state" shapes and experimental observations for B=0, 0.5 and 1 are shown in Fig. 19. One can see that our numerical results match experimental observations quite well, and the numerical interface has a boundary layer near the contact line region, which is consistent with the analysis in [19].

In Fig. 20, the steady state drop shapes for B=0, 0.5, 1 and 1.5 are plotted. We can see that the deformation of drop is large when B is large, which is consistent with the physical

https://doi.org/10.4208/cicp.200114.090316a Published online by Cambridge University Press

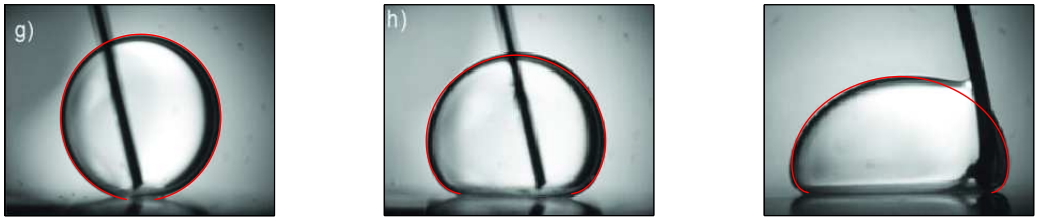


Figure 19: Comparison of equilibrium drop shapes between our "steady state" numerical solutions (red lines) and pictures taken in the laboratory [19].

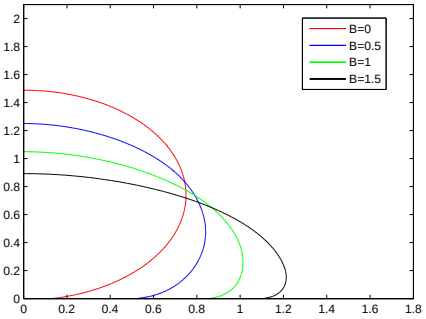


Figure 20: "steady state" (half) drop profiles for B=0, 0.5, 1, and 1.5.

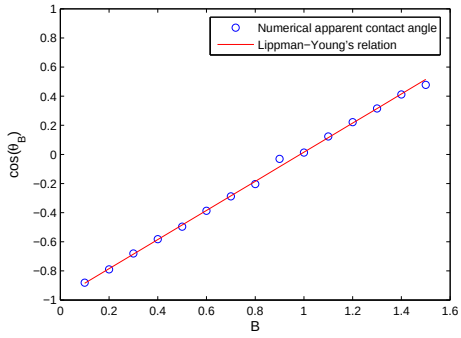


Figure 21: Comparison between numerical apparent contact angles and Lippmann-Young's relation.

underlying principle. Fig. 21 gives comparison between the Lippmann-Young's relation and the apparent contact angle. It can be seen that our result fits the Lippmann-Young's relation quite well. And our numerical results do not show the contact angle saturation phenomena [3, 19], consistent with the results in [33]. To show the dynamic process of the drop motion, we plot the snapshots of drop relaxing from its initial position to the "steady state" shape for B = 1 in Fig. 22.

Finally, we note that Figs. 15-18 indicate that the drop moves to an equilibrium state. However, if we continue the computations for a longer time, numerical instability starts to occur. This is most likely due to the singular electric force at the contact line. We are currently investigate the origin of the instability and our findings will be reported in a followup paper.

6 Conclusions

In this paper, we present a drop dynamic contact line model under the electrowetting actuation by generalizing the approach in [17], which is based on the principle of energy

https://doi.org/10.4208/cicp.200114.090316a Published online by Cambridge University Press

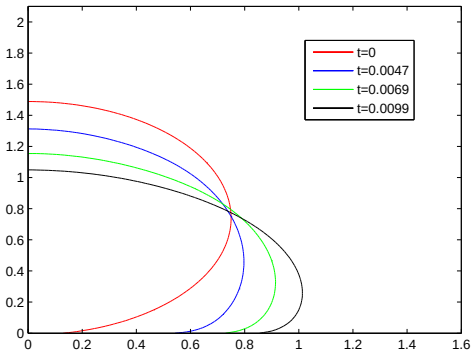


Figure 22: Snapshots of the (half) drop profiles for B$=$1 as it relaxes from its initial position to "steady state".

dissipation. We applied the model to compute the equilibrium shape of a conducting drop on an electrowetting device, and produced some numerical results for the drop motion process under electrowetting actuation. Since the electric field is discontinuous across the drop interface and level set method is a fully Eulerian method, numerically, it is crucial to calculate the electric force acting on the drop interface properly, we use a simple artificial average method to compute the electric force acting on the drop interface and choose the results when the drop first reaches its maximum deformation as our "steady state" numerical results. Our "steady state" numerical results agree well with experimental observations and are consistent with the theoretical analysis, and some preliminary results for drop dynamic motion are obtained.

We now summarize the novel feature of our paper. It is the first time a consistent derivation is given for a moving contact line under electric field. Our derivation is based on the work by [7, 17] without the electric field, which is based on energy dissipation argument. This model reveals that the contact line is not affected by the electric force and the electric force is only acting on the drop interface that away from contact line. Thus the local contact angle of our model is unaffected by the electric field, only the apparent angle is affected by the electric field. This can be seen from (2.2), (2.3) and (2.6). Unlike the previous models [9, 13–15], where the Navier slip conditions are imposed on the whole solid boundary so that slip length needs to be resolved in order to get mesh convergent results, our model shows that the parameter λ on the contact line determines the motion of contact line while the slip length $\lambda_{\pm}$ imposed on solid boundary that away from the contact line has no direct impact, which is confirmed by our numerical results.

Acknowledgments

DH is supported by the Fundamental Research Funds for the Central Universities, the Program for Young Excellent Talents at Tongji University (No. 2013KJ012), the Natural

https://doi.org/10.4208/cicp.200114.090316a Published online by Cambridge University Press

Science Foundation of China (No. 11402174) and the Scientific Research Foundation for the Returned Overseas Chinese Scholars, State Education Ministry. HH is supported in part by NSERC (Canada) and the Fields Institute.

A Derivation of the two-phase axisymmetric model for a conducting drop on an electrowetting device

Following [32], the general 3D electrohydrodynamics equations for an incompressible fluid are given as

$$\rho(\vec{u}_t+\vec{u}\cdot\nabla\vec{u})=-\nabla p+\nabla\cdot\mathbf{T}_\mu+\nabla\cdot\mathbf{T}_e, \tag{A.1}$$

$$\nabla\cdot\vec{u}=0 \tag{A.2}$$

in $\Omega_\pm^*$, where $\mathbf{T}_\mu$ and $\mathbf{T}_e$ are the viscous stress and Maxwell stress tensors, respectively, and Ω_-^* and Ω_+^* are the three dimensional space occupied by water and silicone oil, respectively. For the problem of a conducting water drop immersed in an silicone oil, $\mathbf{E}\equiv 0$ in Ω_-^*, thus

$$\nabla\cdot\mathbf{T}_e=0, \quad \text{in } \Omega_-^*.$$

On the boundary Γ, we have

$$\mathbf{E}_{\vec{\mathbf{t}}}=0, \quad \mathbf{E}=|\mathbf{E}|\vec{n}.$$

Since

$$\mathbf{T}_e=\varepsilon_+\varepsilon_0\left(\mathbf{E}\otimes\mathbf{E}-\frac{|\mathbf{E}|^2}{2}\mathbf{I}\right), \quad \nabla\cdot\mathbf{T}_e=\nabla\cdot(\varepsilon_+\varepsilon_0\mathbf{E})\mathbf{E}=0$$

in Ω_+^*, $\nabla\cdot\mathbf{T}_e$ drops out from Eq. (A.1).

Since the fluid and charge velocities are small in comparison to the velocity of light, magnetic effects due to the motion of charges are negligible [33], the Maxwell equations become

$$\nabla\times\mathbf{E}=0, \quad \nabla\cdot\mathbf{D}=q, \quad \mathbf{D}_t=-\mathbf{J}, \tag{A.3}$$

in region Ω_+^* and Ω_d^*, where $\mathbf{D}=\varepsilon\varepsilon_0\mathbf{E}$ is the displacement vector, $\mathbf{J}=q\vec{u}+\sigma\mathbf{E}$ is the total flux (neglecting charge diffusion), q is the volume charge density, σ is the conductivity, Ω_d^* is the three dimensional space occupied by the solid dielectric layer. For the problem of a conducting drop immersed in silicon oil, we have $q=0$ in Ω_+^*, $\vec{u}=0$, in Ω_d^*, $\varepsilon=\varepsilon_+$, $\sigma=\sigma_+$,in Ω_+^* and $\varepsilon=\varepsilon_d$, $\sigma=\sigma_d$, in Ω_d^*.

The total free energy of the system is given as follows

$$F=\frac{1}{2}\int_{\Omega_-^*\cup\Omega_+^*}\rho|\mathbf{u}|^2dx+\int_{\Gamma_-}(\gamma_--\gamma_+)ds+\int_\Gamma\gamma ds+\frac{1}{2}\int_{\Omega_-^*\cup\Omega_+^*\cup\Omega_d^*}\mathbf{E}\cdot\mathbf{D}dx, \tag{A.4}$$

where $\gamma_\pm$ is the interfacial coefficients between fluid in $\Omega_\pm^*$ and the solid, and $\Gamma_\pm$ are the interfaces between fluid in $\Omega_\pm^*$ and the solid. The dissipation rate of the total free energy

https://doi.org/10.4208/cicp.200114.090316a Published online by Cambridge University Press

in three dimensional space has the following form:

$$\begin{aligned}F_t=&-\int_{\Omega_-^*\cup\Omega_+^*}\mu|\nabla\vec{u}|^2\mathrm{d}x-\int_{\Omega_+^*}\sigma_+|\mathbf{E}|^2\mathrm{d}x-\int_{\Omega_d^*}\sigma_d|\mathbf{E}|^2\mathrm{d}x+\int_{\Gamma_-}\vec{u}\cdot(-p\mathrm{I}+\mathbf{T}_\mu)\cdot\vec{n}\mathrm{d}s\\&+\int_{\Gamma_+}\vec{u}\cdot(-p\mathrm{I}+\mathbf{T}_\mu)\cdot\vec{n}\mathrm{d}s+\int_{\Gamma}\vec{u}\cdot\left([-p\mathrm{I}+\mathbf{T}_\mu]_\Gamma-\gamma\kappa-\frac{\varepsilon_+\varepsilon_0|\mathbf{E}|_+^2}{2}\right)\cdot\vec{n}\mathrm{d}s\\&+\int_l(\gamma_--\gamma_++\gamma\cos\theta_D)u_l\mathrm{d}s,\end{aligned}\tag{A.5}$$

where we have used Eqs. (A.1)-(A.3), aforementioned electric field properties, and the continuity of velocity field. Here l is the contact line, u_l is the (outward) normal velocity of the contact line, $\mathbf{I}$ is the identity matrix, $[f]_\Gamma=f_--f_+$ denotes the jump f across the interface Γ.

Following [17], we assume that energy dissipation occurs only on the fluid-solid interface and on the moving contact line. Using a linear friction law as in [17] and the no-penetration condition $\vec{u}\cdot\vec{n}=0$ on the solid boundary, and taking the axisymmetric property into account, we easily derive the following conditions:

$$\vec{n}\cdot[-p\mathbf{I}+\mathbf{T}_\mu]_\Gamma\cdot\vec{n}=\gamma\kappa+\frac{\varepsilon_+\varepsilon_0|\mathbf{E}|_+^2}{2}\quad\text{on }\Gamma,\tag{A.6}$$

$$\vec{t}_i\cdot[-p\mathbf{I}+\mathbf{T}_\mu]_\Gamma\cdot\vec{n}=0\quad\text{on }\Gamma,\ i=1,2,\tag{A.7}$$

$$\vec{r}\cdot\mathbf{T}_\mu\cdot\vec{n}=-\beta_\pm u,\quad v=0\quad\text{on }\Gamma_\pm,\tag{A.8}$$

$$\gamma_--\gamma_++\gamma\cos\theta_D=-\beta u_l,\quad v=0\quad\text{on the contact line},\tag{A.9}$$

where $u=\vec{u}\cdot\vec{r}$ is the slip velocity in r direction on the solid boundary, $\vec{r}$ is the unit vector in r direction, $\beta_\pm$, β are the friction coefficients on the solid boundary and contact line, respectively.

The dissipation rate of total energy is given by

$$\begin{aligned}F_t=&-\int_{\Omega_-^*\cup\Omega_+^*}\mu|\nabla\vec{u}|^2\mathrm{d}x-\int_{\Omega_+^*}\sigma_+|\mathbf{E}|^2\mathrm{d}x-\int_{\Omega_d^*}\sigma_d|\mathbf{E}|^2\mathrm{d}x-\int_{\Gamma_-}\beta_-u^2\mathrm{d}s\\&-\int_{\Gamma_+}\beta_+u^2\mathrm{d}s-\int_l\beta u_l^2\mathrm{d}s\le 0.\end{aligned}\tag{A.10}$$

Following [23,24], we can recast Eqs. (A.1), (A.2), (A.6) and (A.7) into a level set formulation as follows

$$\rho(\phi)(\vec{u}_t+\vec{u}\cdot\nabla\vec{u})=-\nabla p+\nabla\cdot\vec{T}+\left(\gamma\kappa(\phi)+\frac{\varepsilon_+\varepsilon_0|\mathbf{E}|_+^2}{2}\right)\nabla\phi\delta(\phi),\tag{A.11}$$

$$\nabla\cdot\vec{u}=0\tag{A.12}$$

in $\Omega^*=\Omega_-^*\cup\Omega_+^*$. Here $\vec{T}=\mu(\phi)(\nabla\vec{u}+(\nabla\vec{u})^T)$. Eqs. (2.2), (2.3) and (2.4) are the non-dimensional axisymmetric form of (A.11) and (A.12). And the boundary conditions (2.5) and (2.6) are non-dimensional form of (A.8) and (A.9), where $\cos\theta_0=(\gamma_+-\gamma_-)\gamma^{-1}$ and θ_0 is the static contact angle.

https://doi.org/10.4208/cicp.200114.090316a Published online by Cambridge University Press

References

[1] S.K. Cho, H. Moon and C.-J.Kim, Creating, transporting, cutting, and merging liquid droplets by electrowetting-based actuation for digital microfludic circuits, J. Microelectromechan. Syst, 12 (2003) 70-80.

[2] B. Shapiro, H. Moon, R. Garrell, and C.-J. Kim, "Equilibrium behavior of sessile drops under surface tension, applied external fields, and material variations." J. Appl. Phys., vol.93, 2003.

[3] F. Mugele, and J.-C. Baret, Electrowetting: from basics to applications, J. Phys.: Condensed Matter, 17 (2005) 705-774.

[4] V. Bahadur and S. V. Garimella, Energy Minimization-Based Analysis of Electrowetting for Microelectronics Cooling Applications, J. Microelectron. 39 (2008) 957-965.

[5] Hayes R. A, Feenstra B. J, Video-speed electronic paper based on electrowetting, Nature, 425, 383-385, doi:10.1038/nature01988 (2003).

[6] Srinivasan V, Pamula V. K., Fair R. B., An integrated digital microfluidic lab-on-a-chip for clinical diagnostics on human physiological fluids, Lab Chip 2004, 4, 310-315.

[7] W. Ren and W. E, Boundary conditions for the moving contact line problem, Phys Fluids, 19 (2007) 022101.

[8] J. Li and M. Renardy, Numerical simulation of moving contact line problems using a volume-of-fluid method, J. Comput. Phys. 171 (2001) 243-263.

[9] S. Afkhami, S. Zaleski and M. Sussmann, A mesh-dependent model for applying dynamic contact angles to VOF simulations, J. Comput. Phys. 228 (2009) 5370-5389.

[10] J.-B., Dupont, D. Legendre, Numerical simulation of static and sliding drop with contact angle hysteresis. J. Comput. Phys. 229 (2010) 2453-2478.

[11] H. Huang, D. Liang and B. Wetton, Computation of a moving drop/bubble on a solid surface using a front-tracking method, Comm. Math. Sci. 2 (2004) 535-552.

[12] P.D.M. Spelt, A level-set approach for simulations of flows with multiple moving contact lines with hysteresis, J. Comput. Phys. 207 (2005) 389-404.

[13] Y. Sui, Peter D.M. Spelt, An efficient computational model for macroscale simulations of moving contact lines. J. Comput. Phys. 242 (2013) 37-52.

[14] Y. Sui, Peter D.M. Spelt, Validation and modification of asymptotic analysis of slow and rapid droplet spreading by numerical simulation. J. Fluid Mech. 715 (2013) 283-313.

[15] Y. Sui, H. Ding, and Peter D.M. Spelt, Numerical Simulations of Flows with Moving Contact Lines, Annu. Rev. Fluid Mech. 46 (2014) 97-119.

[16] F. Mugele, Fundamental challenges in electrowetting: from equilibrium shapes to contact angle saturation and drop dynamics, Soft Matter 5 (2009) 3377-3384.

[17] W. Ren, D. Hu and W. E, Continuum Models for the Moving Contact Line Problem, Phys. Fluids 22 (2010) 102103.

[18] M.G. Lippmann, Relations entre les phénomènes electriques et capillaires, Ann. Chim. Phys. 5 (1875) 494-549.

[19] F. Mugele, and J. Buehrle, Equilibrium drop surface profiles in electric fields, J. Phys.: Condensed Matter, 19 (2007) 375112.

[20] C. Scheid, P. Witomski, A proof of the invariance of the contact angle in the electrowetting, Math. Comput. Model. 49 (2009) 647-665.

[21] F. Harlow and J. Welch, Numerical calculation of time-dependent viscous incompressible flow of fluid with free surface. Phys Fluids, 8, 2182-2189, 1965.

[22] Z. Li, M.-C. Lai, G. Wei, H. Zhao, An augmented method for the free boundary problems with moving contact lines. Comput. Fluids, 39 (2010) 1033-1040.

https://doi.org/10.4208/cicp.200114.090316a Published online by Cambridge University Press

[23] C. S. Peskin, The immersed boundary method, Acta Numerica., 11 (2002) 479-517.
[24] Y. C. Chang, T. Y. Hou, B. Merriman and S. Osher, A level Set Formulation of Eulerian Interface Capturing Methods for Incompressible Fluid Flows, J. Comput. Phys., 124 (1996) 449-464.
[25] G.-H. Cottet and E. Maitre, A level set method for fluid-structure interactions with immersed surfaces, MATH. MOD. METH. APPL. S., 16 (2006) 415-438.
[26] G.-H. Cottet, E. Maitre and T. Milcent, Eulerian formulation and level set models for incompressible fluid-structure interaction. ESAIM: M2AN, 42 (2008) 471-492.
[27] G. Jiang and D. Peng, Weighted ENO schemes for Halmiton-Jacobi equations. SIAM J. SCI. Comput. 21 (2000) 2126-2143.
[28] D. He, H. Huang and Y. Tan, Numerical simulation for a droplet fission process of electrowetting on dielectric device. Commun. Comput. Phys. 7 (2010) 1076-1094.
[29] J. J. Xu, W. Ren, A level-set method for two-phase flows with moving contact line and insoluble surfactant, J. Comp. Phys. 263 (2014) 71-90.
[30] D. He, H. Huang, A Constrained Level Set Method for Simulating the Formation of Liquid Bridges. Commun. Comput. Phys., 12 (2012) 577-594.
[31] Z. Li and K. Ito, The Immersed Interface Method: Numerical Solutions of PDEs Involving Interfaces and Irregular Domains. SIAM Frontiers in Applied Mathematics, 33, ISBN-10: 0-89871-609-8 / ISBN-13: 978-0-898716-09- 2, 2006.
[32] A. Castellanos, Electrohydrodynamics, Springer-Verlag, 1998.
[33] C. Eck, M. Fontelos, G. Grn, F. Klingbeil, and O. Vantzos, On a phase field model for electrowetting, Interfaces Free Boundaries, 11 (2009) 259-290.

https://doi.org/10.4208/cicp.200114.090316a Published online by Cambridge University Press